International Journal of Computational and Experimental Science and ENgineering (IJCESEN)

Vol. 11-No.2 (2025) pp. 3624-3639
http://www.ijcesen.com

ISSN: 2149-9144

Research Article

Ensuring Privacy in COVID-19 Detection with Blockchain and Multi-Modal Data Fusion of Breathing Sounds and X-rays

B. Srinivasa Rao[1], G Bala Krishna[*2], M Varaprasad Rao[3], M. Sridevi[4], G Vishnu Murthy[5], G Sravanthi[6]

[1] Professor, Department of Computer Science and Engineering (Data Science), Geethanjali College of Engineering and Technology, Cheeryal, Medchal-501301, Telangana, India.
Email: drbsrinivsarao.cse@gcet.edu.in - **ORCID**: 0000-0001-8845-4303

[2]Associate Professor, School of Engineering, Anurag University, Hyderabad
*** Corresponding Author Email:** Me2balu@gmail.com - **ORCID:** 0000-0002-8714-4159

[3]Department of CSE(DS), CVR College of Engineering,Hyderabad, India
Email: varam78@gmail.com - **ORCID**: 0000-0003-1766-4826

[4]Associate Professor, School of Engineering, Anurag University, Hyderabad
Email: sridevids@anurag.edu.in - **ORCID**: 0000-0002-0226-6430

[5]Professor, School of Engineering, Anurag University, Hyderabad
Email: Gvm189@gmail.com - **ORCID**: 0009-0005-8646-933X

[6]Assistant Professor, Department of CSE ,Malla reddy college of Engineering
Email: sravanthi887@gmail.com - **ORCID**: 0000-0001-5799-6935

Article Info:

DOI: 10.22399/ijcesen.1966
Received : 25 February 2025
Accepted : 16 April 2025

Keywords

COVID-19 Detection
Blockchain Technology
Breathing Sounds
Chest X-ray Imaging
Privacy-Preserving Systems

Abstract:

Current models exhibit a range of shortcomings, such as problems with scaling, increased delays, and prolonged time taken to forecast results. A blockchain based health disease prediction system tackles the below problem by needing a secure model which is able to execute and protect the Machine Learning (ML) and DL strategies utilized for prediction and forecasting diseases accurately without fear of compromise. The traditional approach to health care data management does not secure the information, allows neither data ownership control by patients, nor any data synergy between the stakeholders. This solution seeks to harness blockchain technology's decentralized network, transparency, and encryption of information to efficiently store, process and disseminate health records of patients on top of which DL models are added for accurate disease detection and treatment recommendations.

1. Introduction

AI methodologies are crucial in conjunction with BT since they have completely revolutionized the data processing, analysis, and decision-making capabilities, on the other hand, blockchain provides secrecy, transparency, and integrity. While AI sharpens the accuracy of medical diagnostics, predictive analytics and anomaly detection, blockchain secures sensitive information while making unauthorized access impossible and assures immutability. In healthcare, AI makes deep learning models that analyze medical images while using blockchain to store and share them securely without tampering. Thus, this partnership forms the basis of a great foundation for intelligent, secure, and efficient healthcare systems, with COVID-19 detection and patient data management being the two most promising areas. Data science is the field dedicated to analyzing large volumes of data with advanced tools and techniques to uncover hidden patterns. Leveraging these techniques enables more accurate diagnoses, better patient management and improved public health responses.

2. Parallel Research Work

Detection Of Chest Diseases And COVID-19 Using ML

Salama GM et al. [1] introduced a hybrid model developed for the detection of COVID-19, incorporating both ML and DL methods. This utilized ten unique Deep Convolutional Neural Network (DCNN) systems designed to derive characteristics from CT images. By extracting characteristics derived from various layers of each network, were able to determine the most effective layer for feature extraction for each CNN model. The dataset comprises 2,481 CT images. Yet, CT stands as the crucial imaging test for evaluating COVID-19, offering precision, and faster results, though it also presents elevated misdiagnosis rates.Gupta C et al. [2] introduced an innovative hybrid DL model named COVIDet, which integrates CNNs with the Speeded-Up Robust Features (SURF) extraction technique for the identification of COVID-19. The SURF was employed to extract relevant features, which were subsequently processed by a 25-layer CNN for detection purposes. The hybrid model was compared against established models like VGG19, ResNet50, Inception, Xception and traditional CNN architectures. Nevertheless, the challenge was that RT-PCR, despite being widely used as in inefficient method that takes 5 to 6 hours to complete and often fails to produce results under high demand.Albadr MA et al. [3] designed the Particle Swarm Optimization-Extreme Learning Machine (PSO-ELM) represents an ML algorithm for its effectiveness and rapidity in classification tasks. The voice samples utilized for this enhancement data were acquired from the Corona Hack Respiratory Sound Dataset. (CHRSD). The experimental findings indicated that the PSO-ELM achieved remarkable accuracy for the respective scenarios of deep breathing and shallow breathing. However, most modern systems for the detection of COVID-19 have been developed. been created utilizing a limited dataset. Additionally, Table 2 signifies the evaluation of the detection of chest diseases and COVID-19 monitoring using ML and DL with the existing techniques. Ali AM et al. [4] developed two distinct examinations of the characteristics of capacity and thickness of scratches and denseness identified in the CT images of patients established to have COVID-19, employing structural techniques. The subsequent process involves the classification of pneumonia severity in these patients. These employ modified CNNs alongside the K-Nearest Neighbour (KNN) algorithm and conduct a comparative analysis of the outcomes from both representations in comparison to alternative classification algorithms to ensure accurate identification of lung inflammation. Although, issues in achieving higher accuracy with ensemble CNN compared to kNN and other classification models, while addressing the potential complexity and computational demands associated with ensemble methods.Rao GE et al. [5] presented a hybrid outline designed for the recognition of respiratory lung diseases, which combines traditional convolutional neural networks (CNNs) with quantum classification techniques. It integrates a traditional deep feature extraction model with classification methods based on quantum principles. A new Custom CNN (CCNN) has been introduced specifically for feature extraction, in conjunction with the Multi-Multi-Single (MMS) and Multi-Single-Multi-Single (MSMS) algorithms are categorized as a quantum method. Nevertheless, the challenges in the Quantum Neural Network (QNN) domain address complex problems that were difficult for classical computers.

Table 1 *Comparison of the recognition of chest diseases and COVID-19 monitoring using ML*

References	Methods	Key points	Pros	Cons	Performance metrics used
Salama GM et.al [1]	ML with DCNN	DCNN achieved high accuracy in COVID-19 classification.	Combines the strengths of DL and ML.	Potentially complex integration.	➢ Accuracy ➢ Precision ➢ F1-score
Gupta C et .al [2]	COVIDet with SURF	COVID-19 improves the secured model with high COVID-19 detection accuracy.	Enhanced data security with high performance.	Security integration introduces overhead.	➢ Accuracy ➢ Security metrics
Albadr MA et.al [3]	PSO-ELM with MFCCs	PSO-ELM enhances effective detection with optimized learning.	Fast convergence and reduced training time.	Lack of fine-tuning for stability.	➢ Accuracy ➢ Convergence ➢ Speed
Ali AM et.	CNN with	CNN with KNN provides effectiveness at detecting	TL reduces	May require fine-tuning for	➢ Accuracy ➢ Error rate

al [4]	KNN	pneumonia levels in COVID-19 patients.	training time.	different datasets.	➢
Rao GE et.al [5]	CNN with QNN	QNN improves the accuracy of lung disease detection.	Utilizes quantum computing for enhanced results.	Quantum computing challenges are resource-intensive.	➢ Accuracy ➢ Precision ➢ Recall ➢ F1-score

Table 3. *Comparison of the recognition of chest diseases and COVID-19 monitoring using DL*

References	Methods	Key points	Pros	Cons	Performance metrics used
Talukder MA et al. [6]	DL	DL provides the optimized performance in COVID-19 detection.	High accuracy with reduced overfitting.	Requires extensive computational resources.	➢ Sensitivity ➢ Specificity ➢ Accuracy
Bennour A et.al [7]	MDCXR 3-Net	MDCXR3-Net enhances the effective diagnosis of pulmonary diseases.	High generalization capability.	Data dependency, high computational cost.	➢ F1-score ➢ Recall ➢ Sensitivity
Ramadevi P et.al [8]	DL with CNN	DL provide the hyperparameter tuning improved performance.	Enhanced model precision.	Time-consuming, optimization process.	➢ Accuracy ➢ Precision ➢ AUC
Abdulahi AT et.al [9]	DCNN	DCNN enhances the high accuracy in identifying lung diseases.	Specialized model for pulmonary diseases.	Limited to specific diseases.	➢ Accuracy ➢ Precision ➢ Recall
Srinivas K et. al [10]	Inception V3 and VGG16	Inception V3 and VGG16 demonstrate effective capabilities in predicting COVID-19 over the examination of X-ray images.	Combines advantages of both models.	High computational demands.	➢ Accuracy ➢ Sensitivity ➢ Specificity

2.2 Detection of chest diseases and COVID-19 using DL

Talukder MA et al. [6] explored the possibility of utilizing X-rays, alongside DL algorithms to facilitate the swift and precise identification of patients diagnosed with COVID-19. The suggested methodology enhances detection precision by optimizing specific layers within several well-known TL models. The experiments were carried out using a dataset of X-ray images related to COVID-19 consisting of 2000 images. However, the effective utilization of this dataset requires the specialized knowledge of radiologists to ensure accurate diagnoses of COVID-19 patients.

Bennour A et al. [7] introduced DL models designed for the diagnosis of lung diseases. The first model, known as the COVID-19 Chest X-ray Network (CovCXR-Net) was designed to differentiate between COVID-19 cases and typical cases. The subsequent technique, termed the Multi-Disease Chest X-ray Network (MDCXR3-Net), is capable of identifying COVID-19 and pneumonia, classifying cases were the model known as MDCXR4-Net was developed to detect conditions like COVID-19. Furthermore, it faced challenges in incorporating extra convolutional layers and implementing dropout regulation into the revised architecture of MDCXR3-Net aims to enhance the efficiency of the model. Ramadevi P et al. [7] focused on the optimization of the bayesian method in conjunction of DL with CNN. Furthermore,

employed pre-trained CNN models alongside SVM classifiers to categorize CXR images. An assessment was conducted on the performance of six leading deep pre-trained models in comparison to the efficacy of an optimized CNN, utilizing a chest X-ray image dataset that encompasses categories. However, this technique faces challenges in the multi-class classification involving COVID-19, typical pneumonia, bacterial pneumonia, viral pneumonia and tuberculosis.

Abdulahi AT et al. [9] suggested a model for image detection that is based on DCNN, enhanced through image augmentation techniques, aimed at identifying three distinct pulmonic diseases. This approach is compared to traditional texture descriptor techniques for recognizing This provides the novel DCNN model designed for the specific purpose of enhancing the identification of pulmonary diseases through radiographic imaging. Additionally, the challenge lies in ensuring these supportive organizations effectively complement traditional diagnostic methods.

Srinivas K et al. [10] developed the new hybrid model, referred to as Inception V3, is integrated with the Visual Geometry Group (VGG16), a system created to enhance the prediction of chest X-ray images. This model integrates two DL architectures Inception V3 and VGG16. In the pre-processing phase, images with dissimilar dimensions and color concentrations utilized were recognized and adjusted accordingly. The first block was dedicated to the VGG-16 architecture, while the second and third blocks were associated with the Inception V3 networks. However, ensuring this model consistently distinguishes between coronavirus, normal and viral cases remains challenging. Subsequently, the evaluation of the chest disease and COVID-19 using DL is demonstrated in Table 2.3

3 Proposed Methodologie

The COVID-19 pandemic is a significant issue across the world where millions have suffered from the disease and even lost their lives. This research proposes holistic structure in which multimodal DL methods are applied for early diagnosis and categorization of the symptoms of COVID-19.

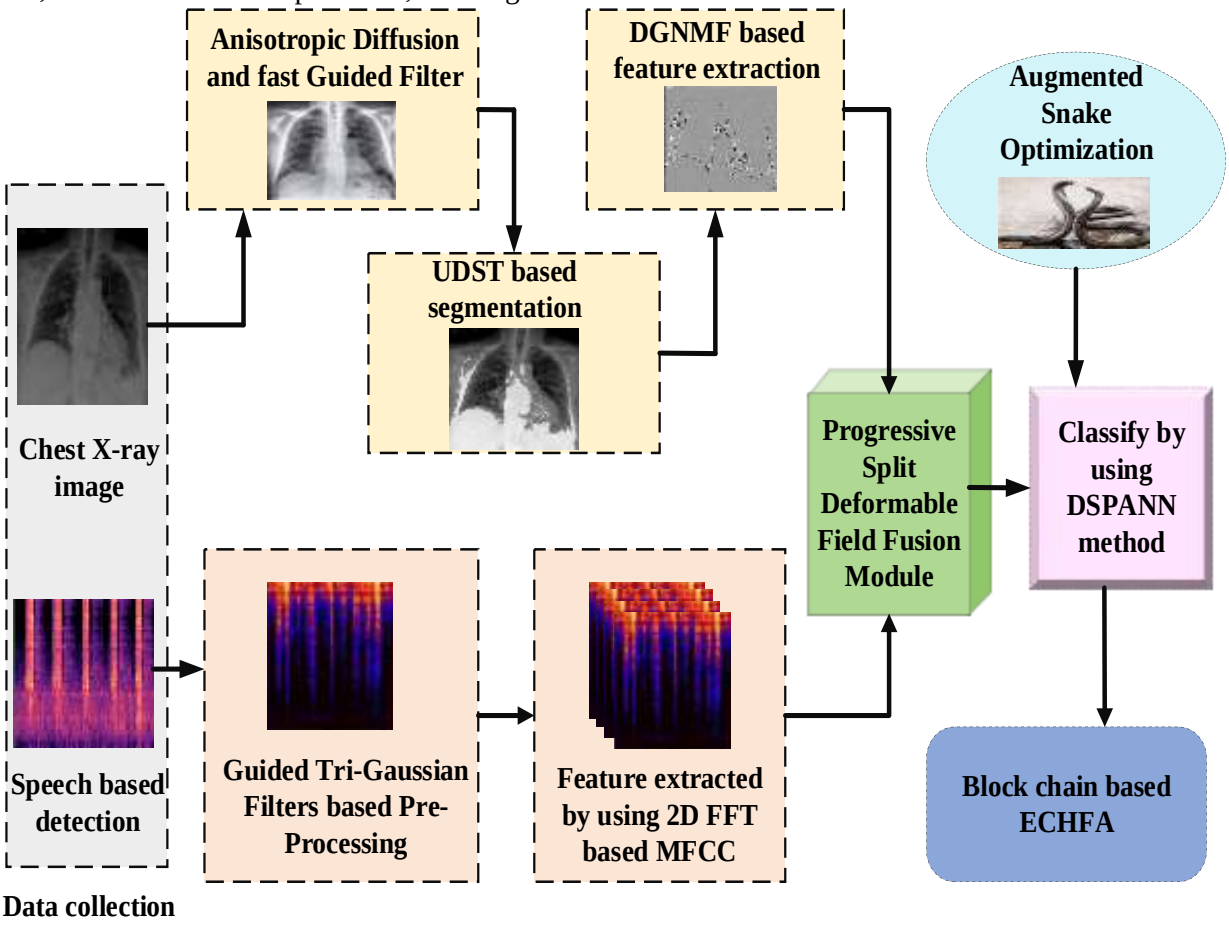

Figure 1. *System architecture of proposed method*

As delineated in Figure 1, the chest x-ray and speech-based models are incorporated within the same model alongside other methods that allow for specific and efficient COVID-19 prediction. To begin, the chest x-ray model increases the predictive quality by performing some enhancing preprocessing techniques and uprated portions are segmented using U shaped Dual Swin attention Transformer (UDST). Deep Graph regularized Nonnegative Matrix Factorization (DGNMF) is utilized to fetch the pertinent features. In the second phase, a modality in which speech is used, employs Guided Tri-Gaussian Filters (GTGF) along with 2 Dimensional (2D) Fast Fourier Transform (FFT) based Mel Frequency Cepstral Coefficients (MFCC). Then, Helix fusion is achieved at the subsequent phase through the use of Progressive Split Deformable Field fusion Module (PSDFM). In addition, the proposed DSPANN employs state-of-the-art convolutional networks for purpose of classification. A blockchain-enabled approach to ECHFA is also introduced to protect data during the global model training where parties cooperate to share their data and learn from each other.

3.1 Phase 1: For chest X-ray image-based detection model

The procedure involved in pre-processing of input adjustments x-ray images with the help of Anisotropic Diffusion and fast Guided Filter (ADGF) [11,12] carries out some mathematical operations to raise the standard of the images and suppress any undesired noise. The preprocess function is shown in Figure 2.

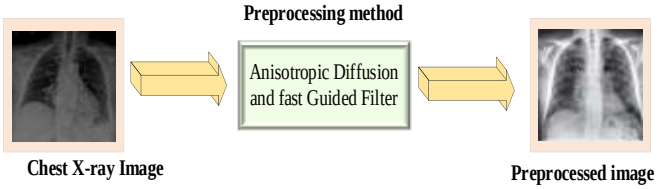

Figure 2. *Workflow of x-ray pre-processing*

The method of anisotropic diffusion intends to raise the standard of images by smoothening the image while taking care to retain the edges. There is a function associated with the rates at which diffusion occurs and it often controls this process which generally expressed in terms of partial differential equation as in equation (1).

$$\frac{\partial M}{\partial T} = \nabla \cdot (r \nabla M) \tag{1}$$

where, M denoted as image; T represented as time; ∇ denoted as gradient operator and r denoted as diffusion rate. The application of the diffusion process preserves the properties of the ordinary scales and also maintains the edge contour information which leads to an enhanced image with better expression of details.

To further improve the image quality, fast guided filter is used in order to avoid blurring of strong edges in the decomposed images. It relies on a local linear basis. The formula for the guided filter is described by the equation (2).

$$f_i = a_i M_i + b_i \tag{2}$$

where, f_i denoted as filtered output; a_i and b_i denoted as linear coefficient and i represents the iterations. The coefficients a_i and b_i are determined through linear regression, and it is expressed in equation (3) and (4).

$$a_i = \frac{\text{cov}(M_i, c_i)}{\text{var}(M_i) + p} \tag{3}$$

$$b_i = \bar{c}_i - a_i \overline{M}_i \tag{4}$$

where, c_i denoted as guided image; $\bar{c}_i$ and $\overline{M}_i$ denoted as the means of c_i and M_i in a local square window, **COV** denotes covariance; var denotes variance and p is the regularization term.

By employing various subsampling rates, an efficient means of edge-preserving smoothing is provided in the fast-guided filter. In the preprocessing phase, the synthesis works for anisotropic diffusion and rapid guided filter enhancement of image quality, noise reduction, and preservation of important structures, especially in chest x-ray images.

U-shaped Dual Swin attention Transformer based segmentation

The UDST [13] takes the pre-processed x-ray images as input. Typically, the U-shaped architecture includes an encoding and a decoding structure. During the encoding phase of the network, the input image is processed in a hierarchical fashion, and features are extracted at various abstraction levels. Figure 3 depicts the flow diagram corresponding to the segmentation performed after pre-processed x-ray image.

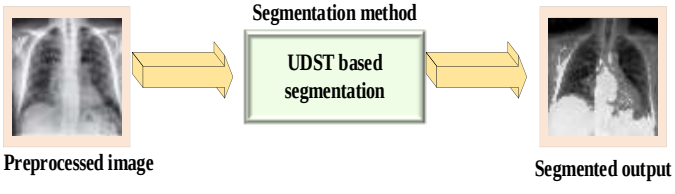

Figure 3. *Process map for x-ray segmentation*

Inside the encoding process of the module, the attention transformer performs to the dyadic Swin attention transformer, where it learns the unique characteristics and details embedded in the given image to appropriately model the long-distance context. The network applies oneself to these portions of the image through attention in order to focus on areas in the image that warrant, extra analysis. In the final part of the U architecture, the decoding stage, attention techniques enhance and focus on important attributes that assists in the segmentation output, filling the segmented output. The last step of the UDST is producing a picture that incorporates particulate quickly segmented regions of different areas of interest, or masking the regions in the chest x-ray that need attention.

Deep Graph Regularized Nonnegative Matrix Factorization based feature extraction

DGNMF is a feature extraction technique that is able to analyse and comprehend complex relations and structures from data, especially for segmented images [14]. The diagram in Figure 4 depicts the flow of feature extraction procedure after segmentation.

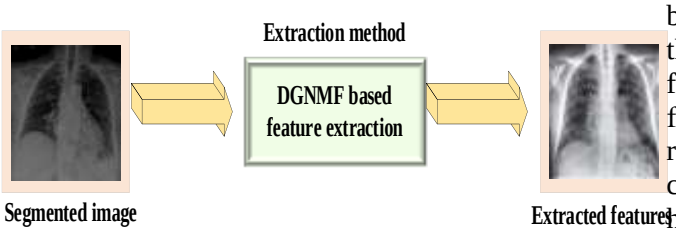

Figure 4. *Flow diagram of x-ray feature extraction*

DGNMF aims to factorize a given segmented image matrix R in to two nonnegative matrices P and Q, while incorporating graph regularization. Mitigating the reconstruction loss alongside maximizing the graph-related continuity as described by equations (5) and (6).

$$R \approx PQ \tag{5}$$

$$\min P \geq 0, Q \geq 0 \left\| R - PQ \right\|^2 Fn + \vartheta \, Ob\,(Q^T Lap\, Q) \tag{6}$$

where, $Ob\,(Q^T Lap\, Q)$ is the objective function, Ob represents trace of matrix, ϑ represents the regularization parameter, Lap is the Laplacian matrix derived from the nearest neighbor graph. Fn is Frobenius norm. The method employs multiplicative update rules to iteratively refine the factorized matrices P and Q. The purpose of these modifications is to reduce the error of reconstruction; however, the graph regularization term is also taken into account and the math representation of it is given in equation (7) and (8).

$$P_{ij} \leftarrow P_{ij} \frac{(RQ^T)_{ij}}{(PQQ^T)_{ij}} \tag{7}$$

$$Q_{ij} \leftarrow Q_{ij} \frac{(R^T Q)_{ij}}{(P^T PQ^T)_{ij}} \tag{8}$$

These updates continue iteravely until convergence, adapting the elements of P and Q to capture relevant features. The goal function in the graph regularization model incorporates a cost for straying from the graph topology, thereby promoting smoothness and continuation of the learned features as depicted in equation (9).

$$Ob(Q^T Lap\, Q) = \sum_{i,j} Lap_{ij} Q_{ij}^2 \tag{9}$$

The Laplacian matrix Lap is constructed based on the nearest neighbour graph, reflecting local geometric relationships in the data.

3.2 Phase 2: Guided Tri-Gaussian Filters based Pre-Processing

A cough, breath and voice signals enhance speech-based model embedded tri-gaussian filters suppress the noise and distortions very efficiently. The filtering process involves employing gaussian functions, which are then used to 'mask' and thus remove unwanted noise elements, resulting in a cleaner representation of the basic signals and a higher quality of the entire signal. The mathematical representation of the tri-gaussian $G(T)$ model is expressed in equation (10).

$$G(T) = A_1 \cdot exp\left(-\frac{(T-me_1)^2}{2sd_1^2}\right) + A_2 \cdot exp\left(-\frac{(T-me_2)^2}{2sd_2^2}\right) + A_3 \cdot exp\left(-\frac{(A-me_3)^2}{2sd_3^2}\right) \tag{10}$$

where, A_i, me_i and sd_i represent amplitude, mean, and standard deviation of the Gaussian component.

The fundamental speech-based model serves as the basis of the tri-gaussian model, thereby introducing some flexibility to the concept of filtering. This is mathematically expressed in equation (11). The guided filter weight parameters are obtained by examining the local linearity between the guided graph $u(T)$ and filtered outputs $f(T)$.

$$f(T) = \sum_i O_i \cdot u(T_i) \tag{11}$$

The coefficients O_i are optimized based on a cost function that minimizes the difference between input and output in each window. The adaptive filtering process employs tri-gaussian parameters and attributes improvement of sound quality to

noise suppression distortion elimination and component selection.

Two-dimensional Fractional Fourier Transform based Mel Frequency Cepstral Coefficient feature extraction

After carrying out the necessary steps to clean the audio signal, it is subjected to a critical two-dimensional FFT operation, which results in a transformation of the signal to the fractional frequency domain [15,16]. This is also considered as the step in MFCC extraction from audio signals where time-frequency representation is already be converted to the fractional frequency region. The orders ϕ and η are important in determining the direction and type of this transformation. By varying these values, certain frequency bands are focused on and the signal is better represented in the following processing steps.

The 2D FFT of a two-dimensional signal $Z(c,d)$ with orders ϕ and η is expressed in equation (12).

$$X_{\phi,\eta}[Z](p,q) = \int_{-\infty}^{\infty} Z(a,d)U_{\phi,\eta}(c,d;p,q)\,dc\,dd \tag{12}$$

where, $X_{\phi,\eta}$ represents the function of X with parameters applied to another function Z with variables p and q. The integration is carried out over the entire range from $-\infty$ to ∞.

The 2D FFT kernel $U_{\phi,\eta}(c,d;p,q)$ is expressed in equation (13).

$$U_{\varphi,\eta}(c,d;p,q) = exp\left(-j\left[\frac{\pi}{2}(\varphi c^2 + \eta d^2) + \frac{\pi}{2}(\varphi p^2 + \eta q^2)\right]\right) \tag{13}$$

where, j represents the imaginary unit.

Once the 2D FFT has applied to the signal, the next step involves filtering the signal with Mel frequency shaped triangular bandpass filter panels, which imitates human sense of hearing. Next, the filtered values are squeezed logarithmically to store the information pertaining to the extent to which the sounds are perceived as loud. Conclusively, the log values compressed by the filter are decorrelated using the Discrete Cosine Transform (DCT) producing MFCC, which are very useful coefficients of feature extraction audio for recognition and processing purposes.

3.3 Phase 3: Progressive Split Deformable Field Fusion Module

The PSDFM, is an apparatus developed for the purpose of fusing disparate modalities including, for instance, chest x-ray scans and their corresponding audio signals. The schematic diagram of fusion and classification is presented in Figure 5.

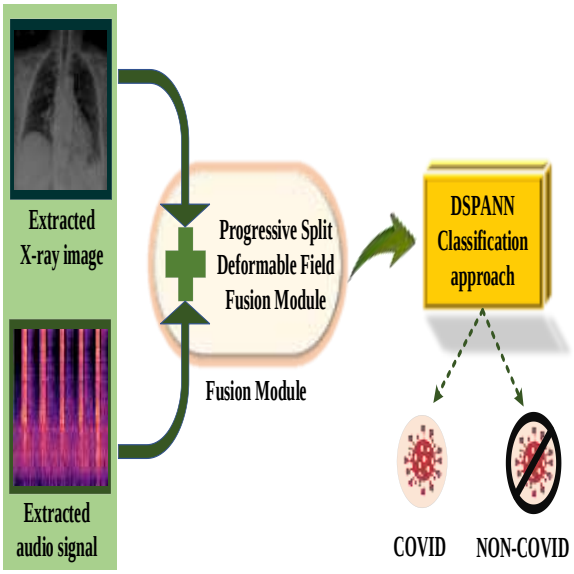

Figure 5. *Proposed fusion approach*

Deformable Field Fusion is a process in which the features taken some breast x-ray images and some audio signals - are not combined - they are cut or deformed in some way. Deformable fusion allows adaptable alignment of features from various modalities by accommodating to the changes in scale or orientation among others. This flexibility adds to the effectiveness of feature fusion yielding a richer representation.

Progressive Fusion means that the merging of elements does not happen instantaneously but takes place over a period of time and through a number of stages or steps. There is an exclusive distinction among each step of the process of fusion where the information from different modalities is conglomerated. Each step introduces new operations to the fused representation thereby improving it. Also, this provides a way to ventilate different aspects of information and improve on a multimodal representation. The main function of PSDFM is expressed by equation (14).

Let Y_{X-ray} is the extracted features of x-ray image and Y_{audio} is the extracted features of audio

$$Intermediate\,Y_1 = Split\,(Y_{X-ray}, Y_{audio})$$
$$Deformed\,Y_1 = Deform\,(Intermediate\,Y_1)$$
$$Intermediate\,Y_2 = Split\,(Deformed\,Y_1)$$
$$Deformed\,Y_2 = Deform\,(Intermediate\,Y_2)$$
$$.$$
$$.$$
$$.$$
$$Fused\,Y = We_{sum}\,(Deformed\,Y_n) \tag{14}$$

where, Y represents features; We_{sum} denotes weighted sum of fused features and Y_n represents the n^{th} features. The procedure is carried out in an iterative manner, including the breakdown and alteration of the features drawn from chest radiographs and auditory data. The last fused features are obtained through the weighted summation of deformed features.

- **Dual Sampling Dilated Pre-Activation Residual Attention Convolution Neural Network based classification**

To categories the combined features, the DSPANN method [16] is used. Classification of images with significant improvement in accuracy is achieved by using Multi Dilated Convolution (MDC), Pre-Activation Residual Convolutional (PARC) and Dual-Sampling Attention (DSA) network as the building blocks of the network. The structure of DSPANN is illustrated in Figure 6.

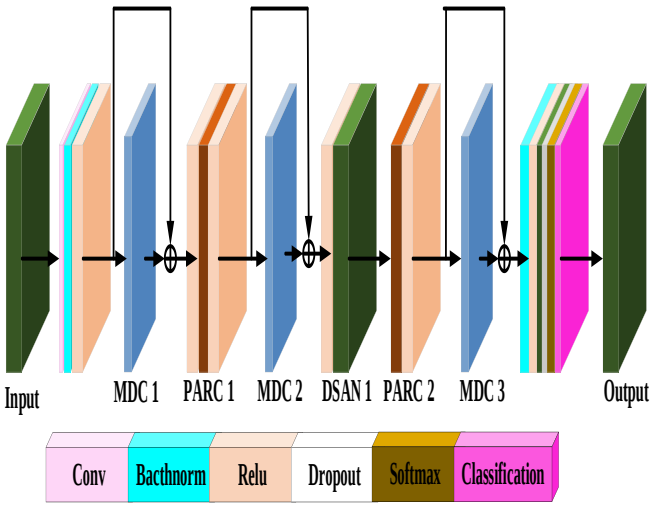

Figure 6. *DSPANN architecture*

Multi dilated convolution

This allows for enhancement of the information perception range of the network without any additional complexity. A dilation factor is, quite simply, the introduction of gaps among the elements of a given convolution kernel in order to increase the receptive field of the network. Typically, convolutional layers work within a smaller fixed spaced arrangement; however, dilated convolution takes advantage of an extra wider span, hence covering a larger area in sample feature extraction without the addition of more parameters. This serves to increase the receptive field at different dilation levels enabling the approach for identifying the correlations and intricate details in the input details both in close range and at a distance. The math model for MDC is as given in the equation (15) below.

$$J(i)=\sum_{n=0}^{n-1}\alpha(n)\cdot J_{in}(i+d\cdot n) \quad (15)$$

where, $J(i)$ represents the output at position i after applying MDC; J_{in} represents the input at position i; $\alpha(n)$ denotes the convolutional kernel weight at position n and d denotes the dilated factor. The addition of different locations of the kernel n allows the network to use information from a larger area in terms of the receptive field.

Pre-Activation Residual Convolutional

The PARC overcomes the issue of redundancy in the inputs from spectral bands by applying a Squeeze-and-Excitation (SE) block for channel attention and feature recalibration in an effort to focus on the important features. The design and components of the architecture include 3-D Global Average Pooling (GAP), 3D convolutional layers, ReLU, and a sigmoid function, and the attention weight is applied following the convolution and preceding the summation in the residual block. The output of PARC is represented in equation (16).

$$Z(J(i))=act\left(R(J(i))+J(i)\right) \quad (16)$$

Where, $Z()$ represents the output of residual block, act represents the activation function and R represents the residual learning function.

Dual-Sampling Attention Network

The model is based on the 3D Residual Network 34 (ResNet34) architecture which uses 3D convolutional kernels and incorporates a last residual block with stride 1, which allows for reconstructing high-quality feature maps just before GAP. 3D Class Activation Mapping (CAM)-based attention generates normalized attention maps that soft masks images using convolution $1\times1\times1$ and ReLU activations followed by a sigmoid function for easy masking. The forward-response sampling solves the imbalanced existing infections challenge; training two branches, one with uniform and the other with balanced-paired response sampling. The outputs of both branches are integrated through a dual sampling approximation scheme. In order to enhance the relevant performance metrics, a variant of snake optimization known as Augmented Snake Optimization (ASO) [154] seeks to effectively

manage the search process by an appropriate degree of exploration and exploitation.

Initialization:

The ASO technique works by first initializing a population of snakes. For the purpose of this, random locations of the individuals are generated within an interval (defined by $R_{\max}$ and $R_{\min}$). The initialization is mathematically formulated as shown in equation (17).

$$R_j = R_{\min} + l \times (R_{\max} - R_{\min}) \quad (17)$$

where, R_j denotes j^{th} individual position and l is a random number (0,1).

Dividing the Swarm into Two Equal Subsets:

The count of snakes is divided evenly into two categories; females and males. Use equations (18) and (19) to cluster the swarm.

$$E_a \approx E/2 \quad (18)$$

$$E_c = E - E_a \quad (19)$$

where, E represents the entire number of participants, E_a denotes the quantity of male participants, and E_c denotes the quantity of female individuals.

Evaluate Each Group and Characterize Temperature and Food Measure:

The most fit member (in terms of fitness) of each group is located by using equation (20). The temperature (Te) is found by employing an exponential decay formula with respect to the current iteration (It) and a fixed maximum iteration count (Co).

$$Te = \exp\left(\frac{-It}{Co}\right) \quad (20)$$

Food quantity (Q) is defined using with the exponential equation (21), where, h_1 is equals 0.5.

$$Q = h_1 * \exp\left(\frac{It - Co}{Co}\right) \quad (21)$$

Exploration Phase:

If $Q < 0.25$ (0.25 is a threshold value) is reached, the snakes commence looking for the food by selecting arbitrary location, and assessing the respective coordinates. This is known as exploration in the model, and the mathematical representation is given by equation (22).

$$R_{j,a}(It+1) = R_{rand,a}(It) \pm h_2 \times M_a \times ((Rminmin_{max} \quad (22)$$

where, $R_{j,a}$ denotes the position of the j^{th} male, $R_{ran,a}$ represents the position of a randomly selected male, $rand$ denotes random number (0,1), and M_a signifies the male's ability to locate food.

Exploitation Phase:

If $Q > Thershold$ condition is met and the temperature exceeds 0.6 (which is regarded as hot) the snakes only approach the food using the equation (23).

$$R_{j,i}(It+1) = R_{food} \pm h_3 \times Te \times rand \times \left(R_{food} - R_{j,i}(It)\right) \quad (23)$$

where, $R_{j,i}$ denotes the location of a participant (male/female), R_{food} represents the location of the best individual, and h_3 is set to 2. If the temperature drops below the defined limit indicating a cold condition, the snake enters either the fight/mating mode in accordance with the mathematical formulations captured in equations (24) and (25).

$$R_{j,n}(It+1) = R_{j,n}(It) + h_3 \times FM \times rand \times rand \times \left(Q \times R_{best,c} - R_{j,a}(It)\right) \quad (24)$$

where, $R_{j,a}$ denotes the location of a male, $R_{best,c}$ signifies the leading member's rank in the female population and FM is the male agents fighting ability.

$$R_{j,c}(It+1) = R_{j,c}(It+1) + h_3 \times FF \times rand \times \left(Q \times R_{best,a} - R_{j,c}(It+1)\right) \quad (25)$$

where, $R_{j,c}$ represents the female position, $R_{best,,a}$ represents the best individual position of the male group, and FF is the female agents fighting ability. Additionally, K_a and K_c represent the mating ability of the male and female, calculated using equations (26) and (27).

$$K_a = \exp\left(\frac{-s_{i,c}}{s_{i,a}}\right) \quad (26)$$

$$K_c = \exp\left(\frac{-s_{i,a}}{s_{i,c}}\right) \quad (27)$$

In case eggs are hatched, select the least adapt male and female and substitute them into the equations (28) and (29) respectively.

$$R_{worst,a} = R_{\min} + rand \times \left(R_{\max} - R_{\min}\right) \quad (28)$$

$$R_{worst,c} = R_{\min} + rand \times \left(R_{\max} - R_{\min}\right) \quad (29)$$

where, $R_{worst,a}$ refers to the lowest quality participant within the male category, whereas $R_{worst,c}$ denotes the lowest quality participant in the female category.

Termination:

The process of the method is repeated by alternating between exploration and exploitation until some termination criteria are reached, such as performing a prescribed iterative cycle or achieving a certain fitness level. The diagram of ASO is given in Table 3.

Table 3: ASO algorithm

Start by randomly generating the individuals in the population.

Split the population E into two equal segments E_a and E_c using (18) and (19).

while $(It < Co)$ do

Measure each group E_a and E_c

Identify the optimal male and female

Specify temperature according to (20) and Describe food quantity based on (21)

if $Q < 0.25$ then

Conduct investigation with (22)

else if $(Q > 0.6)$ then

Carry out exploitation (23)

else

if $rand > 0.6$ then

Snakes in aggressive posture (24) and (25)

else

snakes in mating mode (26) and (27)

Modify the worst-performing male and female through (28) and (29)

end if

end if

end while

Provide optimal solution

The combination of the snake optimization method with a classification technique serves the purpose of selecting the optimal parameters or features in order to maximize the classification ability. The algorithm uses a combination of exploration and exploitation strategies to search the parameter space in an efficient manner, thereby minimizing the overall complexity of the classification task.

3.4 Blockchain based Encrypted Crypto Hash Federated Algorithm

In another healthcare data-sharing situation, the proposed method guarantees privacy-preserving cooperation among more than one hospital with the use of federated learning [15]. While model training is made private, blockchain technology has made it possible to share models without the fear of violating any patients' privacy. Except for the very few wealthy hospitals which is able to afford external cloud storage, most hospitals only keep their own CT scan data and look up the weights of trained models in the blockchain. A new hospital's joining transaction in the blockchain gives this last data ownership verification, together with specific types and sizes of data it owns. The blockchain also has all the hospitals' unique identification numbers. In this way the distance among location of the nodes (hospitals) d for the data query according to the categories K is calculated by Equation (30).

$$d_p(L_p, L_q) = \frac{\sum_{i,j\in\{L_p \cup L_q - L_p \cap L_q\}} \left(r_{ij}^{Lp} + r_{ij}^{Lq}\right)}{\sum_{ij\in L_p \cup L_q} \left(r_{ij}^{Lp} + r_{ij}^{Lq}\right)} \cdot log\left(d_i(L_p, L_q)\right) \quad (30)$$

where, $r_{ij}^{K_p}$ This represents a value associated with the relationship between hospital i and hospital j for category L_p, $\sum_{i,j\in\{L_p \cup L_q - L_p \cap L_q\}} \left(r_{ij}^{L_p} + r_{ij}^{L_q}\right)$ is the sum of the values associated with the relationships between hospitals i and j for

categories L_p and L_q , excluding the intersection of L_p and L_q.

The mathematical representation to generates unique IDs (id) for nodes to maintain privacy is expressed in equation (31).

$$d(L_p, L_q) = L_p(id) \oplus L_q(id) \quad (31)$$

The randomized approach explained in equation (32) provides data privacy for each of the two hospitals.

$$Kr[F(N) \in R] \leq \exp(a) \cdot Kr[F(N') \in out \quad (32)$$

Where, N and N' represents the neighbouring records, out denoted as outcome of data, $F(N)$ is a function that operates on the data set N. Kr represent a measure of privacy risk or a privacy metric. a represent a constant or a threshold controlling the level of privacy. R indicates the acceptable or expected output range.

In order to protect sensitive data u_p, Laplace mechanism is employed (equation (33)).

$$\hat{u}_p = u_p + laplace(x/a) \quad (33)$$

Sensitivity (x) is computed to evaluate the level of Laplace noise (equation (34)).

$$x = \max_{L,L'} \left\| f(L) - f(L') \right\| \quad (34)$$

Where, $f(L)$ transformation applied to the input data L. The consensus protocol enables the training of global models by capitalizing on the use of local models. Nodes also offer proof of work as a means of ensuring safe data dissemination. In the training period, the coordination algorithm evaluates the performance of local models in terms of Mean Absolute Error (MAE), as expressed in equation (35).

$$MAE(u_p) = \frac{1}{n} \sum_{p=1}^{n} \left| v_p - f(z_i) \right| \quad (35)$$

where, v_p actual value, n total number of data points. $f(z_i)$ denotes the predicted value from the model for the i^{th} instance or input z_i. The joint decision-making approach, often referred to in case of health facilities as the voting approach, is articulated in a mathematical form and given in equation (36).

$$MAE(L_q) = \mu \cdot MAE(u_p) + \frac{1}{n} \sum MAE(u_p) \quad (36)$$

All data transactions are encrypted and signed using public and secret keys. In the distributed ledger approved records are systematically stored, MAE is in charge of transactions. In the place of sending original data, hospitals exchange secure locally trained model weights over the blockchain. Proposed system architecture enables training of the global model μ across multiple hospitals. This development is necessary for protocols that deal with uneven datasets from different hospitals as they have to be amalgamated efficiently. This process involves formulating node selection as a function that maximizes the quality of the resultant global model built after aggregation subject to considerations of model size and time cost. The ECHFA which has developed is based on smart contracts and blockchain architecture addresses issues such as patient privacy, promotes collaborative learning and helps keep the trained models in a safe decentralized environment.

4 Results and Discussion

This research employs Python as the programming platform for carrying out the image processing experiments. The experiments are executed on a personal computer with high-end specifications consisting of 3.40 GHz CPU, 16GB RAM supported by an Intel Core i7-6700 CPU which offers sufficient processing power. To carry out a comprehensive assessment the developed databases have been processed into two portions; training set (80% of the database) and a test set (20%). Such a partitioning strategy helps in effective testing and validation of the methodologies adopted. Indeed, the suggested configuration employs the chest x-ray as well as audio sample information of the COUGHVID dataset towards correct early diagnosis of COVID-19. It contains 2,800 coughs with rich participant details that are labelled by experts. The chest x-ray repository holds 13,808 entries out of which 80% are used for training and 20% for testing. 10% of the training set, chosen at random, is employed for validation of the model. This exhaustive strategy helps to train, test and validate ML models for COVID-19 prediction very effectively.

The COUGHVID dataset exhibits potential biases such as reliance on self-reported COVID-19 statuses, leading to inaccuracies in labelling. Variability in recording quality due to different devices and environments impacts model training. Additionally, demographic imbalances, including overrepresentation of certain age groups, genders, or regions, may limit the generalizability of the model.

4.1 Experimental results of proposed approaches

This research has incorporated advanced techniques of image processing for preprocessing segmentation and feature extraction of x-ray images. The results of the x-ray images are shown in Figure 7.

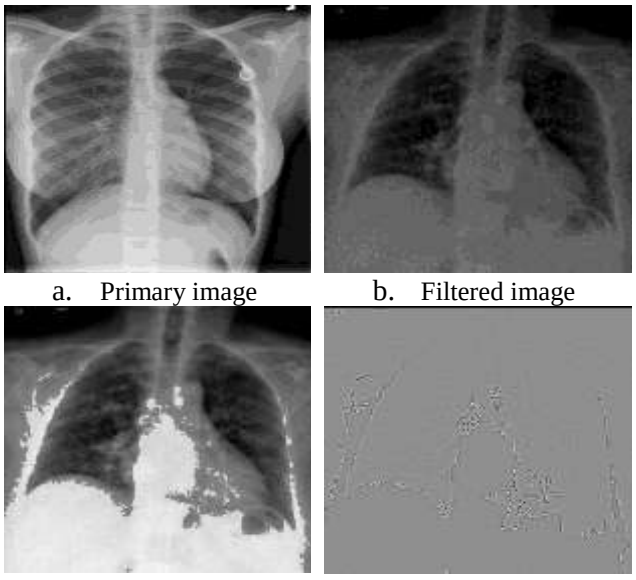

a. Primary image b. Filtered image

c. Segmented image d. Retrieved

Figure 7. *Pre-processed, segmented, extracted images of chest x-ray*

As anisotropic diffusion is applied to the images, noise is eliminated while some of the important features are enhanced resulting to a quality image. Fast guided filter is used to improve the images further, this time without threatening the edges and the small details. The outcome achieved from this preprocessing step was well improved with respect to clarity and noise control. UDST based segmentation method is above others in terms of complex patterns and contours found in x-ray images. The attention mechanism ensured that the network focused only on relevant regions hence contributing to achieving good segmentation which is also robust. The segmented images presented structures of interest which are used in the analyses that followed. DGNMF method improves the feature extraction capabilities of the segmented image regions through the application of graph regularization which captures the spatial relationships between the different regions. DGNMF is able to find different textures, shapes and patterns in the segmented areas effectively and created a succinct and meaningful description of the x-ray images.

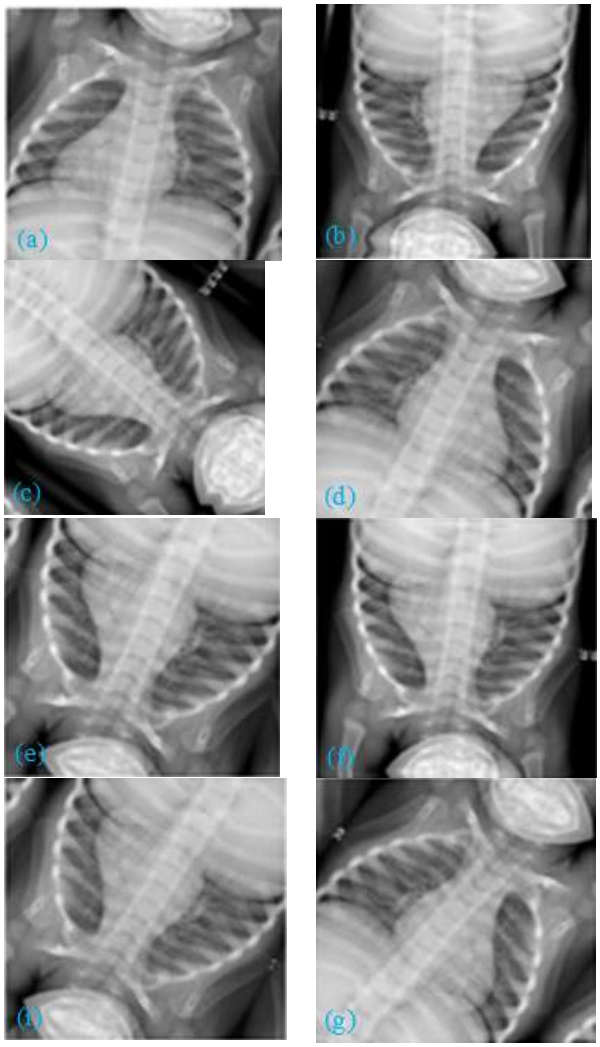

Figure 8. *DSPANN classification process*

The outcome of the classification process using a DSPANN is depicted in Figure 8. To obtain features from the input images, DSPANN employs multi dilated convolution. This approach progressively increases the area of the receptive field to capture features of varying sized while not significantly increasing parameters.

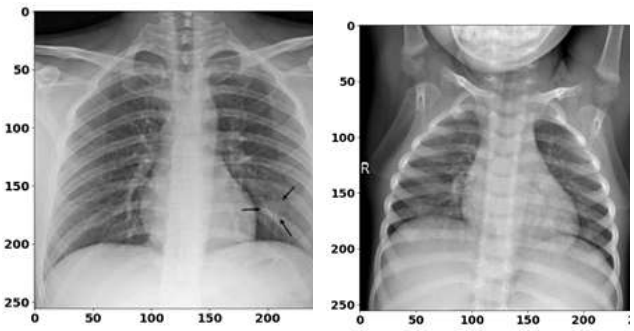

(a) COVID (b) Non COVID

Figure 9. *Predicted outcome of DSPANN approach*

In the end, the model classifies the samples as COVID or Non-COVID. Figure 9 shows the predicted outcome of the DSPANN.

Figure 10 summarizes the results from the blockchain-based ECHFA approach in a detailed way. This novel approach assures the safe and private transfer of data between several hospitals networked together over a decentralized network. To improve security and maintain data authenticity, the ECHFA technique utilizes blockchain and hash codes. Data for each hospital is hashed to produce a unique compression of the data known as a fingerprint. In addition, an ID for each hospital is recorded in the system in the form of a blockchain which further strengthens the decentralized approach.

Figure 10. *The outcome of blockchain-based ECHFA*

Table 4: *Evaluation criteria of the proposed approach*

Evaluation criteria	Accuracy	Precision	Recall	Specificity	F1 score	AUC	MSE	RMSE	MAE
Obtained values (%)	98	98.07	98	98	96.07	97	0.02	0.1414	0.02

Table 4 provides outcomes for the adopted DSPANN approach and reaches an accuracy of 98%. Its precision of 98.07% measures the proportion of correctly diagnosed cases over all the suspected patients while the remaining false cases are minimized, while recall (98%) measures the effectiveness of the system in detecting all the positive instances of a given disease, in particular COVID-19. Specificity (98%) shows the capability of the test to correctly classify the negatives (non-positive cases) without mislabelling them as false negatives. The F1-score (96.07%) is used to gauge performance in tasks which involve the precision and recall weight of left and right components. Area Under Curve (AUC) obtaining is 97% classifies the ability to distinguish the two categories very well. Due to very low Mean Squared Error (MSE) which is rated in 0.02, Root Mean Squared Error (RMSE) of 0.1414 and MAE also rated in 0.02, the predictions made by the model are very precise. Statistical testing follows a straightforward process by formulating a null hypothesis assuming no real difference, choosing a significance level α within (0,1) and defining a test measure Z with an assumed probability distribution $P(Z \mid H_0)$ under the null hypothesis [24,25]. Using this distribution, chance of encountering a test statistic equally or more extreme value z, resulting in the p-value given by $p = 2\min\{P(Z \le z \mid H_0), P(Z \ge z \mid H_0)\}$. If p is less than α then reject H_0, concluding statistical significance. Rejecting a true null hypothesis as a Type I error, and a Type II error involves failing to reject a false null hypothesis, with the risk of a Type I error controlled by α. To comprehensively evaluate model performance, are assessed using one test set. McNemar's test is used for assessing sensitivity and specificity, while DeLong's test

evaluates the AUC, the t-test and Wilcoxon test estimate their differences. Additionally, the F-test, Bartlett's test, and Levene's test determine whether variances exhibit considerable differences illustrated in Table 5. The median and standard deviation of Dice computed from the binary classification are 0.484 and 0.300.

Table 5: Statistical analysis of the proposed approach

Test	Value
McNemar's test	p-value < 0.0207
DeLong test	p-value = 0.137
T-test	p-value = 0.00064
Wilcoxon test	p-value = 0.0012
F-test	0.182
Bartlet test	0.182
Levene test	0.0337

4.2 Comparison of proposed method with existing approaches

The efficiency of the suggested classification model DSPANN is evaluated in comparison existing, namely Long Short-Term Memory (LSTM) [17], Weighted Sum Function (WSF) [18], Convolutional Neural Network (CNN) [19], and Ensemble Monte Carlo Dropout (EMCD) [160], proving that it is more effective.

The accuracy of each method is presented in comparison in the graph shown in Figure 11. LSTM shows lower accuracy, mostly ranging between 70% and 80%, indicating suboptimal performance. WSF demonstrates moderate accuracy, clustering around 85% to 90%. CNN and EMCD exhibit improved accuracy, with most values above 85%. The proposed DSPANN model achieves the highest accuracy, consistently reaching 98% and above, highlighting its superior reliability and effectiveness. This visualization confirms that the DSPANN model outperforms existing methods, making it a more robust and accurate approach for classification tasks.

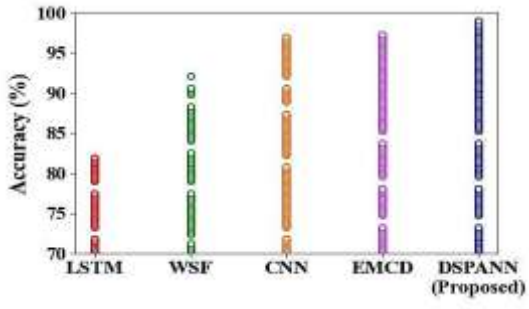

Figure 11. *Accuracy comparison*

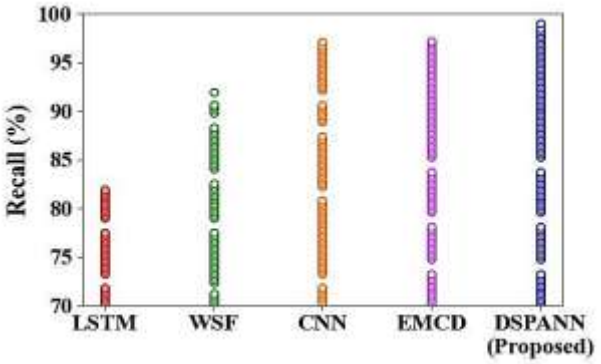

Figure 12. *Recall comparison*

A comparative analysis of the accuracies demonstrates that the highest accuracy at 98% is attained while employing the DSPANN method. Further developments of the model include the dual sampling, dilated convolutions and attention mechanisms which aid in demonstrating strong and reliable classification of COVID-19 infections which denotes its effectiveness in performing accurate detection of such diseases. The comparison of the recall for the methods shown in Figure 12. The recall of an LSTM network equals 81.36%, while that of WSF approximates 97.12%. For CNN, the proposed model obtains 91.8%, EMCD gives 95.78%, and finally DSPANN model gives the best recall being 98.07%.

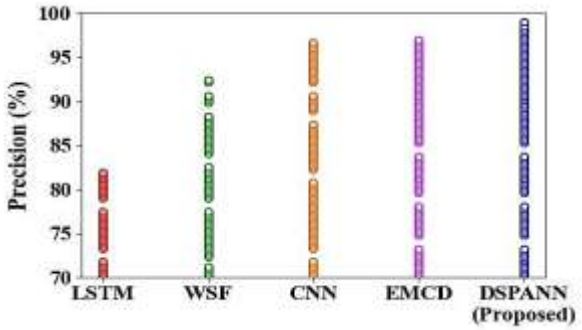

Figure 13. *Precision comparison*

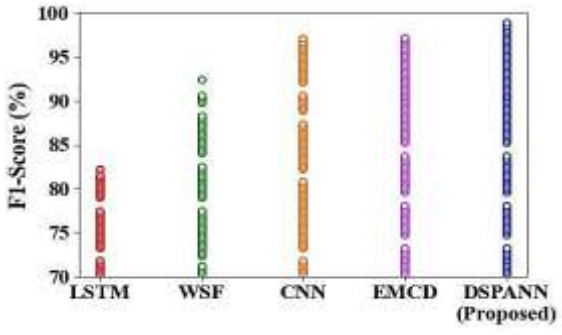

Figure 14. *F1-score comparison*

The precision of each method is visually articulated in Figure 13. It shows that the precision for LSTM model is 80.98%, whereas 97.26% for WSF model, 93.2% in the case of CNN model, 95.12% for EMCD model. Most remarkably, the DSPANN approach is activated with the highest precision of 98%. This comparison strongly indicates that DSPANN is very effective in reducing false positive cases and finding every positive case in the classification of medical images.The F1-score comparison of all the methods has represented in Figure 14. As for the LSTM model, its F1-score is found to be 81.25%, which shows that an equilibrium has reached between precision and recall. WSF obtains a remarkably high F1-score with a value of 96.76%, advocating effectiveness of this technique that has managed to blend precision and recall. F1 scores for CNN and EMCD models are 91.24% and 96.1% respectively. The presented approach DSPANN yields an F1 score of 96.07%, demonstrating its ability to achieve high recall and high precision for medical image prediction of COVID-19. Time and space complexity comparison using existing optimization algorithms like Particle Swarm Optimization (PSO) [18] and Ant Colony Optimization (ACO) [19] is illustrated in Table 6.

Table 6. *Time and space complexity comparison*

Input (samples)	PSO		ACO		ASO (proposed)	
	Time (ns)	Memory usage (kb)	Time (ns)	Memory usage (kb)	Time (ns)	Memory usage (kb)
500	871771	1432.3	89012	1379.81	76078	1048.2
1000	153427	3279.25	162198	3412.45	142106	3176.43
1500	312189	4512.78	321079	4623.76	309543	4431
2000	504678	5043.67	514238	5145.12	498123	4768.65

This comprehensive strategy tackles the issues surrounding COVID-19 detection, while also emphasizing the protection of information.

Conclusion

Taking into consideration x-ray images and breathing sounds together, the multimodal system developed achieves a remarkable 98% accuracy of recognition, 97.02% specificity, and 98% sensitivity. Another key aspect is the privacy solution based on ECHFA on the blockchain, which allows training the model collaboratively while considering restrictions for instance, data privacy in the medical services sector. The results of employing DSPANN and ASO demonstrate the enhancement in classification accuracy while controlling the increase in computational requirements. This research work provides a solution to relevant problems that exist in disease prediction systems by creating a safe, accountable, and confidentiality-ensuring approach. Further objectives must be translated to real life and progressive enhancement of this groundbreaking initiative for it to be more effective on the world's health systems. Also, the accuracy of disease prediction and personalization of healthcare could be improved by looking into other more advanced ML and DL approaches.

Author Statements:

- **Ethical approval:** The conducted research is not related to either human or animal use.
- **Conflict of interest:** The authors declare that they have no known competing financial interests or personal relationships that could have appeared to influence the work reported in this paper
- **Acknowledgement:** The authors declare that they have nobody or no-company to acknowledge.
- **Author contributions:** The authors declare that they have equal right on this paper.
- **Funding information:** The authors declare that there is no funding to be acknowledged.
- **Data availability statement:** The data that support the findings of this study are available on request from the corresponding author. The data are not publicly available due to privacy or ethical restrictions.

Reference

[1] Salama GM, Mohamed A, Abd-Ellah MK. (2024) COVID-19 classification based on a deep learning and machine learning fusion technique using chest CT images. *Neural Computing and Applications*. 36(10):5347-65.

[2] Gupta C, Khan V, Srikanteswara R, Gill NS, Gulia P, Menon S. (2024) A Novel Secured Deep Learning Model for COVID Detection Using Chest X-Rays. *Journal of Cybersecurity and Information Management (JCIM)* 14(01):227-44.

[3] Albadr MA, Tiun S, Ayob M, Al-Dhief FT. (2024) Particle swarm optimization-based extreme learning machine for covid-19 detection. *Cognitive Computation.* 16(4):1858-73.

[4] Ali AM, Ghafoor K, Mulahuwaish A, Maghdid H. (2024) COVID-19 pneumonia level detection using deep learning algorithm and transfer learning. *Evolutionary Intelligence*. 17(2):1035-46.

[5] Rao GE, Rajitha B, Srinivasu PN, Ijaz MF, Woźniak M. (2024) Hybrid framework for respiratory lung diseases detection based on classical CNN and quantum classifiers from chest X-rays. *Biomedical Signal Processing and Control.* 88:105567.

[6] Talukder MA, Layek MA, Kazi M, Uddin MA, Aryal S. (2024) Empowering covid-19 detection: Optimizing performance through fine-tuned efficientnet deep learning architecture. *Computers in Biology and Medicine*. 168:107789.

[7] Bennour A, Aoun NB, Khalaf OI, Ghabban F, Wong WK, Algburi S. (2024) Contribution to pulmonary diseases diagnostic from X-ray images using innovative deep learning models. *Heliyon.* 10(9).

[8] Ramadevi P, Das R. (2024). An extensive analysis of machine learning techniques with hyper-parameter tuning by Bayesian optimized SVM kernel for the detection of human lung disease. *IEEE Access*.

[9] Abdulahi AT, Ogundokun RO, Adenike AR, Shah MA, Ahmed YK. (2024) PulmoNet: a novel deep learning based pulmonary diseases detection model. *BMC Medical Imaging*. 24(1):51.

[10] Srinivas K, Gagana Sri R, Pravallika K, Nishitha K, Polamuri SR. (2024) COVID-19 prediction based on hybrid Inception V3 with VGG16 using chest X-ray images. *Multimedia Tools and Applications*. 83(12):36665-82.

[11] Ho, T.T., Tran, K.D. and Huang, Y., (2022). FedSGDCOVID: Federated SGD COVID-19 detection under local differential privacy using chest X-ray images and symptom information. *Sensors*, 22(10);3728.

[12] Zhang, L., Shen, B., Barnawi, A., Xi, S., Kumar, N. and Wu, Y., (2021). FedDPGAN: federated differentially private generative adversarial networks framework for the detection of COVID-19 pneumonia. *Information Systems Frontiers*, 23(6);1403-1415.

[13] Nguyen, D.C., Ding, M., Pathirana, P.N., Seneviratne, A. and Zomaya, A.Y., (2021). Federated learning for COVID-19 detection with generative adversarial networks in edge cloud computing. IEEE *Internet of Things Journal*, 9(12);10257-10271.

[14] Kumar, R., Kumar, J., Khan, A.A., Ali, H., Bernard, C.M., Khan, R.U. and Zeng, S., (2022). Blockchain and homomorphic encryption-based privacy-preserving model aggregation for medical images. *Computerized Medical Imaging and Graphics*, *102*,102139.

[15] Nassif, A.B., Shahin, I., Bader, M., Hassan, A. and Werghi, N., (2022). COVID-19 detection systems using deep-learning algorithms based on speech and image data. *Mathematics*, *10*(4), p.564.

[16] Kumar, S., Chaube, M.K., Alsamhi, S.H., Gupta, S.K., Guizani, M., Gravina, R. and Fortino, G., (2022). A novel multimodal fusion framework for early diagnosis and accurate classification of COVID-19 patients using X-ray images and speech signal processing techniques. *Computer methods and programs in biomedicine*, *226*, 107109.

[17] Li, S., Li, W. and Li, Y., (2022). Adversarial Graph Regularized Deep Nonnegative Matrix Factorization for Data Representation. *IEEE Access*, *10*, pp.86445-86457.

[18] Bhalke, D.G., Rajesh, B. and Bormane, D.S., (2017). Automatic genre classification using fractional fourier transform based mel frequency cepstral coefficient and timbral features. *Archives of Acoustics*, *42*.

[19] Wang, D., Liu, J., Ma, L., Liu, R. and Fan, X., (2023). Improving Misaligned Multi-modality Image Fusion with One-stage Progressive Dense Registration. *arXiv preprint arXiv:2308.11165*.

[20] Ma, Y., Xu, S., Jiang, T., Wang, Z., Wang, Y., Liu, M., Li, X. and Ma, X., (2023). Learning a Deep Attention Dilated Residual Convolutional Neural Network for Landslide Susceptibility Mapping in Hanzhong City, Shaanxi Province, China. *Remote Sensing*, *15*(13), p.3296.

[21] Khurma, R.A., Albashish, D., Braik, M., Alzaqebah, A., Qasem, A. and Adwan, O., (2023). An augmented Snake Optimizer for diseases and COVID-19 diagnosis. *Biomedical signal processing and control*, *84*, p.104718.

[22] Wang, F., Wang, X. and Sun, S., (2022). A reinforcement learning level-based particle swarm optimization algorithm for large-scale optimization. *Information Sciences*, 602;298-312.

[23] Zhou, X., Ma, H., Gu, J., Chen, H. and Deng, W., (2022). Parameter adaptation-based ant colony optimization with dynamic hybrid mechanism. *Engineering Applications of Artificial Intelligence*, 114;105139.

[24] Rainio O, Teuho J, Klén R. (2024)Evaluation metrics and statistical tests for machine learning. *Scientific Reports.* 14(1):6086.

[25] Elshewey AM, Abed AH, Khafaga DS, Alhussan AA, Eid MM, El-Kenawy ES. (2025)Enhancing heart disease classification based on greylag goose optimization algorithm and long short-term memory. *Scientific Reports.* 15(1):1277.